Hybrid experimental-numerical characterization of the effect of strain rate on fracture

Contents

Abstract

Tensile experiments are carried out on a TRIP780 steel sheet at low ($\dot{\varepsilon} \sim 10^{-3} s^{-1}$), intermediate ($\dot{\varepsilon} \sim 1 s^{-1}$) and high strain rates ($\dot{\varepsilon} \sim 10^3 s^{-1}$). The experimental program

---

includes notched as well as uniaxial tension specimens. Local displacements and surface strain fields are measured optically in all experiments using Digital Image Correlation. Constitutive equations derived from the Mechanical Threshold Stress theory are proposed to describe the rate-dependent behavior as well as plastic anisotropy of the sheet material. Detailed Finite Element simulations of all experiments reveal that the model accurately predicts experimental results, including force displacement curves and local surface strain evolution. In particular, the behavior at large strain, beyond the onset of necking, is well predicted. Stress and strain histories where fracture initiates are also obtained from the simulations in order to characterize the dependence of the material ductility to both strain rate and stress state. If the fracture strain is higher at high strain rate in all experiments, results show that the effect of strain rate on ductility cannot be considered independently from the state of stress.

4.1   Introduction

The plastic deformation behavior of AHSS steels under uniaxial tension has been extensively studied during the last decade, indicating that this class of material experiences positive strain rate sensitivity (e.g. Khan et al., 2012, [91]). Experiments in the intermediate range of strain rates (1 - 10s^{-1}) are typically carried out in servo-hydraulic testing machines (e.g. Huh et al., 2008, [82]) while high strain rate experiments (100 – 1,000s^{-1}) are usually performed in Split Hokinson bar systems (e.g. Van Slycken et al., 2007, [182]; Dunand et al., 2013, [47]) or direct impact setups (e.g. He et al., 2012, [76]). A key advantage of uniaxial tension experiments is that they give a direct access to the material response at small strain levels, and especially to the dependence of flow stress to strain rate. Indeed, force and local displacement measurements are straightforwardly related to the stress and strain within the range of uniform elongation. Used in conjunction with optical strain measurement methods, it also permits to evaluate the effect of strain rate on plastic anisotropy of AHSS sheets (e.g. Huh et al., 2013, [83]). With the exception of a few experimental results reported for shear loading conditions (e.g. Rusinek & Klepaczko., 2001, [155]; Peirs et al., 2011, [147]), virtually no data can be found in the literature describing the multi-axial behavior of AHSS sheets at high rates of strain.

The effect of strain rate on the ductility of AHSS has comparatively been less evaluated. Most experimental investigations are limited to characterizing uniaxial tension parameters such as the ultimate elongation (e.g. Olivier et al., 2007, [141]; Huh et al, 2008, [82]), thereby putting aside the effect of stress state on ductile fracture. Results presented do not permit to draw a clear trend in the dependence of ultimate elongation to strain rate for AHSS steels. Kim et al. (2013, [94]) measured increasing ultimate elongations for increasing strain rates (ranging from $0.1s^{-1}$ to $200s^{-1}$) in case of a DP780 and a TRIP780 steel. Similarly an elongation twice higher at $1000s^{-1}$ than at $0.001s^{-1}$ is found for a TRIP steel by Verleysen et al. (2011, [185]). On the other hand, Wei et al. (2007, [189]) report decreasing ultimate elongations with increasing strain rates in case of two different TRIP-aided steels, while Curtze et al. (2009, [40]) find almost the same elongation at $10^{-3}s^{-1}$ and $750s^{-1}$ for both DP600 and TRIP700 steels. It is emphasized that the ultimate elongation in a uniaxial tension experiment is a structural characteristic and not an intrinsic material property. It depends strongly on the specimen geometry (Verleysen et al., 2008, [184]; Sun et al., 2012, [168]) and is thus a questionable indicator of material ductility. A somewhat more reliable evaluation of the fracture strain in uniaxial tension experiments may be obtained by measuring the reduction of the cross-section area on fractured specimens and assuming a uniform strain distribution through the sheet thickness. Based on this Reduction of Area method, Kim et al. (2013, [94]) report a decreasing fracture strain for increasing strain rates in case of a TRIP780 steel, and a non-monotonic dependence of ductility to strain rate for DP780 steel.

In most fracture experiments on sheet materials, however, the localization of plastic deformation through necking cannot be avoided and represents a major difficulty in the accurate characterization of the material state at fracture. After necking, the stress and strain fields within the specimen gage section become non-uniform and of three-dimensional nature (stresses in the thickness direction develop). Consequently, the stress history prior to fracture can no longer be estimated from the force history measurements using simple analytical formulas: stress and strain histories prior to fracture need to be determined in a hybrid experimental-numerical approach (Dunand & Mohr, 2010, [48]). In other words, a detailed finite element analysis of the experiment is required to identify the stress and strain fields up to the onset of fracture.

The plasticity model used in the numerical simulation is one of the key elements controlling the accuracy of the method.

An extremely wide variety of constitutive equations describing the rate- and temperature-dependent plastic behavior of metals have been proposed. The goal of constitutive equations is to relate the flow stress to strain, strain rate and temperature (and possibly other internal variables) in order to describe the basic mechanisms of strain hardening, strain rate sensitivity and thermal softening (and possibly damage, phase transformation, texture evolution...). Rate-dependent plasticity models can be categorized into two main branches. On the one hand phenomenological models are based on the separation of the effects of strain, strain rate and temperature (e.g. Johnson and Cook, 1983, [88]; Cowper and Symonds, 1952, [39]). Strain hardening, strain rate sensitivity and thermal softening mechanisms are described by means of basic functions, depending respectively on strain, strain rate and temperature only, which may be arbitrarily combined in additive or multiplicative manners to build an ad-hoc model. A partial review of phenomenological basic functions can be found in Sung et al. (2010, [169]). Integrated phenomenological models in which variables are not separated have also been proposed. They allow for description of more complex mechanisms: temperature-dependent strain hardening (e.g. Sung et al., 2010, [169]), rate-dependent strain hardening (e.g. Khan et al., 2004, [93])... On the other hand, attempts have been made to incorporate a description of the mechanisms of plasticity into physics-based constitutive models (e.g. Zerilli and Armstrong, 1987, [195]; Follansbee and Kocks, 1988, [58]; Voyiadjis and Abed, 2005, [187]; Rusinek et al., 2007, [157]). Most physics-based models make use of the theory of thermally activated plastic deformation to relate flow stress, strain rate and temperature (Conrad, 1964, [38]; Kocks et al., 1975, [95]). Additional internal variables can also be introduced in the constitutive equations to account for history effects (Bodner and Partom, 1975, [20]; Durrenberger et al., 2008, [52]). Comparisons between phenomenological and physics-based models against experimental data tend to show that the latter offer better predictive capabilities when a wide range of strain rates and/or temperatures is considered (Liang and Khan, 1999, [111]; Abed and Makarem, 2012, [2]; Kajberg and Sundin, 2013, [90]).

When dealing with sheet materials, plasticity model calibration is usually done based on uniaxial tension experiments in the range of uniform elongation, as experimental measurements give direct access to stress, strain and strain rate. The material behavior at large strains (beyond uniform elongation) is then assumed by extrapolating the strain hardening at low strains with analytical functions (e.g. Hollomon, 1945, [79]; Swift, 1952, [170]; Voce, 1948, [186]…). This extrapolation may lead to inaccurate predictions of the material behavior at large strains. Sung et al. (2010, [169]) calibrated six different hardening functions for a DP780 based on the uniaxial data in the range of uniform elongation. Even though all models fit the data correctly, significant differences are reported at large strains: most extrapolated models did not represent accurately the material behavior beyond uniform elongation.

In this chapter, tensile experiments are carried out at low, intermediate and high strain rates to characterize the rate-dependent behavior of a TRIP780 steel. In addition to uniaxial tension specimens, the experimental program includes tensile specimens with circular notches. Experiments at high strain rates are performed in the Split Hopkinson Pressure Bar system described in Chapter 3. Constitutive equations adapted from the Mechanical Threshold Stress model (Follansbee and Kocks, 1988, [58]) are proposed to model the dependence of the material behavior to strain rate, as well as plastic anisotropy. After calibration using an inverse method, the predictive capabilities of the model are assessed over multiple strain rates and stress states through detailed Finite Element Simulations of all the experiments. A very good agreement is found between numerical and experimental results. In particular, accurate predictions of the post-necking behavior of the sheet material are obtained. A hybrid experimental-numerical approach is taken to characterize the dependence of ductility to strain rate and stress state. It is found that the TRIP material exhibits a higher ductility at high strain rates. However the evolution of ductility between low and intermediate strain rates depends on the stress state.

4.2   Experimental program

4.2.1   Tensile experiments at low and intermediate strain rate

Tensile experiments are performed on straight specimens (Fig. 4-1a) and on flat specimens with circular cutouts (Fig. 4-1c and 4-1d). The specimen loading axis is always oriented along the rolling direction. All specimens are extracted from the sheet material using waterjet cutting. Notched specimens are 20mm wide and feature a b=10mm wide notched gage section. Specimens with two different notched radii are prepared: R=20mm and R=6.65mm. Experiments are carried out in a servo-hydraulic testing machine under displacement control, specimens being hold by friction in custom-made high pressure clamps. The force applied to the specimen is measured by a MTS 250kN static load cell, while displacements and strains in the gage section are measured by Digital Image correlation, as detailed in Section 4.2.4. Two ranges of strain rates are investigated. For low strain rates, a constant crosshead velocity of 0.84mm/min is imposed to the straight specimens, while a velocity of 0.5mm/min is chosen for notched specimens. To reach intermediate strain rates, velocities of 22mm/s and 8.3mm/s are selected for the straight and notched specimens, respectively. All experiments are carried out at room temperature. Note that the static load cell used is not correctly dimensioned for intermediate strain rate experiments, leading to noticeable oscillations in the force measurements (about 1.2% of the measured signal in amplitude) as visible in Figs. 4-2 to 4-4.

4.2.2   Tensile experiments at high strain rate

The modified Split Hopkinson Pressure Bar system (SHPB) presented in chapter 3 is used to performed high strain rate tensile experiments. In all experiments presented here, the compressive stress pulse has a total duration of 550μs and a rise time of about 30μs, its magnitude being controlled by the striker velocity. A specifically designed load-inversion device is used to transform the compressive loading pulse into tensile loading of the specimen gage section. During deformation of the specimen, the load is transmitted through the load-inversion device as a compressive stress wave into the

Figure 4-1: Uniaxial tension specimens for (a) low and intermediate strain rate and (b) high strain rate experiments, tensile specimens with a notched radius of (c) 6.65mm and (d) 20mm. Red dots depict the location of the reference points used to measure displacements.

output bars. The specimen is hold by friction in the load-inversion device, the gripping pressure being applied by 8 M5 screws. The force applied to the specimen gage section is derived from elastic waves propagating in the output bars (Eqn. 3-6), while displacements and strains in the specimen gage section are measured by means of high speed imaging and digital image correlation. The reader is referred to Chapter 3 for more details on the experimental set-up and testing procedure.

High strain rate experiments are performed on uniaxial tension specimens, as well as notched tensile specimens with notch radii of R=20mm and R=6.65mm. Note that the geometry of the uniaxial specimen, sketched in Fig. 4-1b, is different from the one used at low and intermediate strain rates. The gage section is shorter (l=15mm instead of 20mm) and narrower (w=5mm instead of 10mm). On the other hand, the gage section geometry of the notched tensile specimens is the same at low and high strain rate. A series of experiments are performed on the three geometries at room temperature with striker velocities of ranging from 4m/s to 14m/s.

4.2.3 Local displacements and strain measurements

In all tensile experiments, pictures of the specimen surface are recorded to perform optical-based displacement and strain measurements. For that purpose a thin layer of white matt paint is applied to the specimen surface along with a black speckle pattern of a speckle size of about 70μm.

In low strain rate experiments, an AVT Pike F505B with 90mm macro lenses takes about 300 pictures (resolution of 2048x1024 pixels) before the onset of fracture. The camera is placed at 1.5m from the specimen surface, resulting in a square pixel edge length of 23μm. In intermediate and high strain rate experiments, a high speed video system (Phantom v7.3 with 90mm macro lenses) is used. For intermediate strain rate experiments, it operates at a frequency of 1kHz with an exposure time of 50μs. A resolution of 800x600 pixels is chosen. The camera is positioned at a distance of about 400mm from the specimen surface (square pixel edge length of 55μm). In high strain rate experiments the acquisition frequency is set to 100kHz with a exposure time of 2μs, limiting the spacial resolution to 560x32 pixels. The camera is positioned at a

distance of about 550mm from the specimen surface (square pixel edge length of 70μm).

The virtual extensometer function of the digital image correlation software VIC2D (Correlated Solutions, SC) is used to determine the relative displacement of two reference points located on the axis of symmetry of the specimen gage sections. For this, a quadratic transformation of a 23x23 pixel neighborhood of each point is assumed. Spline-cubic interpolation of the grey values is used to achieve sub-pixel accuracy. The position of the DIC reference points on the specimen surface is shown in Fig. 4-1 with solid red dots. For notched tensile specimens, an initial spacing between the reference points of $\Delta x = 30mm$ is used to compute the relative displacement imposed to the specimen, while surface strains at the center of the gage sections are calculated with an initial spacing of $\Delta x = 1mm$. For uniaxial tension, a value of $\Delta x = 11.5mm$ (resp. $\Delta x = 6.6mm$) is chosen at low and intermediate strain rates (resp. high strain rate). Based on the relative displacement Δu of the two reference points, the engineering axial surface strain is computed as

$$\varepsilon = \frac{\Delta u}{\Delta x} \qquad\qquad (4\text{-}1)$$

4.3   Experimental results

4.3.1   Uniaxial tension

Figure 4-2 depicts the engineering stress-strain curves measured under uniaxial tension in the three ranges of strain rates. The instant of fracture is indicated with a solid dot. For low and intermediate strain rates (in black and red in Fig. 4-2, respectively) the onset of fracture corresponds to a sudden drop of the specimen load carrying capacity. In the high strain rate experiment, however, the force level decreases smoothly to zero. The instant of the onset of fracture is therefore identified from the DIC pictures as the instant at which a first crack appears on the specimen surface. In all three experiments, a maximum of force corresponding to the onset of localization of the plastic flow (i.e. necking) is observed. Note that the necking strain decreases as strain
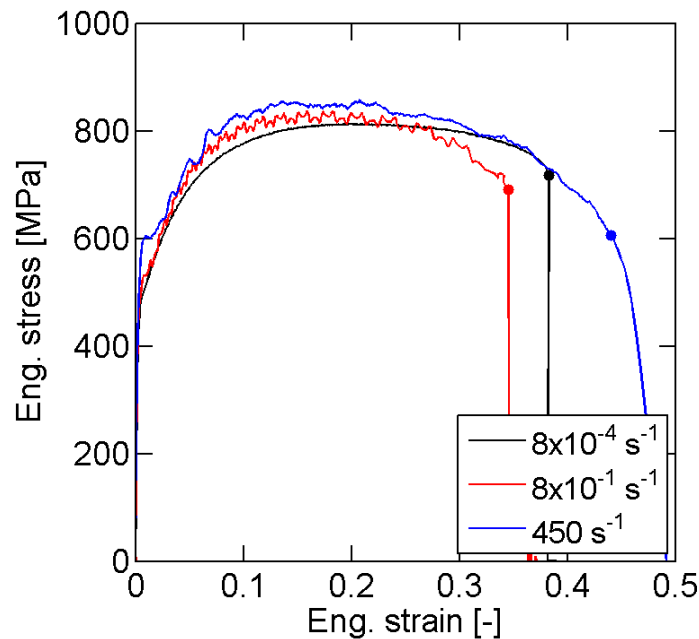
Figure 4-2: Experimental engineering stress-strain curves under uniaxial tension. Results for low strain rates are shown in black, intermediate strain rates in red and high strain rates in blue. Solid dots correspond to the onset of fracture.

rate increases. Necking occurs at an engineering strain of about 0.2 at low strain rate (black curve in Fig. 4-2) while it is only 0.14 at high strain rate (blue curve in Fig. 4-2). For each experiment, a pre-necking strain rate is defined as the time-average of the axial plastic strain rate (measured by DIC) between initial yielding and the onset of necking. A pre-necking strain rate of $\dot{\varepsilon} = 8.10^{-4}\ s^{-1}$ is measured for the experiment at low strain rate (black curve in Fig. 4-2), $\dot{\varepsilon} = 8.10^{-1}\ s^{-1}$ for intermediate strain rate (red curve in Fig. 4-2) and $\dot{\varepsilon} = 450\ s^{-1}$ for high strain rate (blue curve in Fig. 4-2). Note that after the onset of necking, stress and strain fields are no longer uniform in the specimen gage section. Therefore engineering stress and strains should be interpreted as normalized forces and displacements, which are structure-level measurements, rather that local stress and strain measures.

The plastic behavior of the sheet exhibits a weak dependency to strain rate. Both the initial yield stress and strain hardening are rate-sensitive. The material has the same initial yield stress but a higher hardening modulus at intermediate strain rate than at low strain rate. In addition it has a higher initial yield stress but approximately the same

initial hardening modulus at high strain rate than at low strain rate. Before necking, the stress level is about 100MPa higher in the high strain rate experiment than at low strain rate. Note that a comparison of the post-necking part of the curves is not meaningful as different specimen geometries have been used.

4.3.2   Notched tension

Experimental results for the tensile specimen with 20mm notch radii and 6.65mm notch radii are presented in Fig. 4-3 and Fig. 4-4, respectively. Force displacement curves for the three strain rates are depicted in Figs. 4-3a and 4-4a, while the evolution of the engineering axial surface strain at the center of the gage section are plotted in Figs. 4-3b and 4-4b. The onset of fracture is indicated by a solid dot on all curves. As for uniaxial tension experiments, it corresponds to a sharp drop of force in low and intermediate strain rate experiments (in black and red in Figs. 4-3a and 4-4a, respectively), and to the appearance of the first surface crack in the high strain rate experiment (in blue in Figs. 4-3a and 4-4a). Note that surface strain measurements are not available for the high strain rate experiment. Very high strains reached at the center of the gage section combined with high rates of deformation lead to cracking and unsticking of the painted pattern used for correlation.

For the 20mm notched specimen, the relative velocities measured between the two DIC reference points (red points in Fig. 4-1c) are 0.5mm/min for the low strain rate experiment, 8mm/s for the intermediate strain rate experiment and 7.0m/s for the high strain rate experiment, respectively. For the 6.65mm notched specimen, the relative velocities are 0.5mm/min for the low strain rate experiment, 8mm/s for the intermediate strain rate experiment and 4.5m/s for the high strain rate experiment, respectively. Note that the reference point locations are the same in all experiments.

Regardless of the geometry or strain rate, all force-displacement curves feature a maximum of force which corresponds approximately to the onset of localization of the plastic flow in-plane and through the thickness of the sheet (Dunand & Mohr, 2010, [48]). Because of the notched geometry, necking always occurs at the center of the gage section. After the onset of necking, the specimen experiences a loss of load carrying capacity until fracture occurs. With the 20mm notched specimen (Fig. 4-3a), the loss of
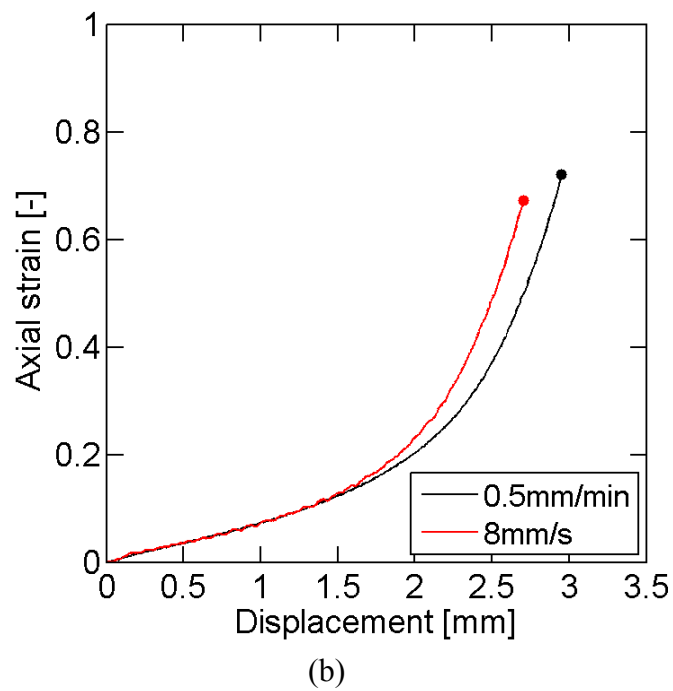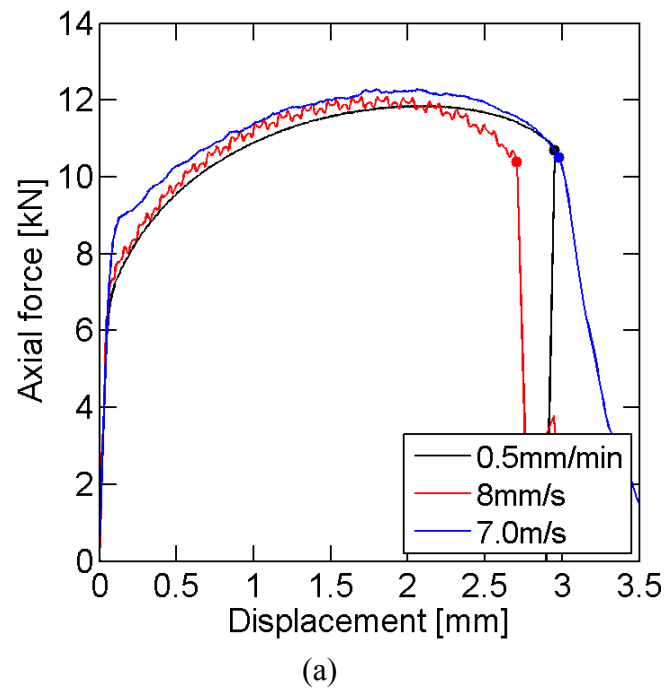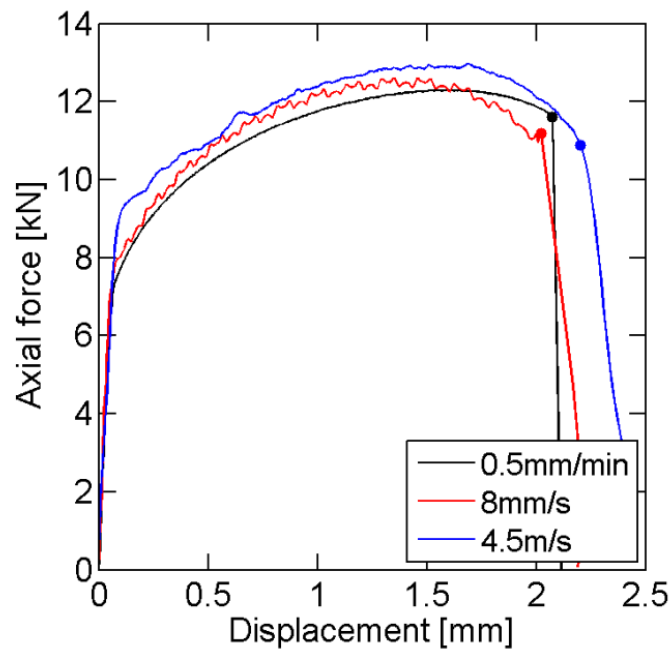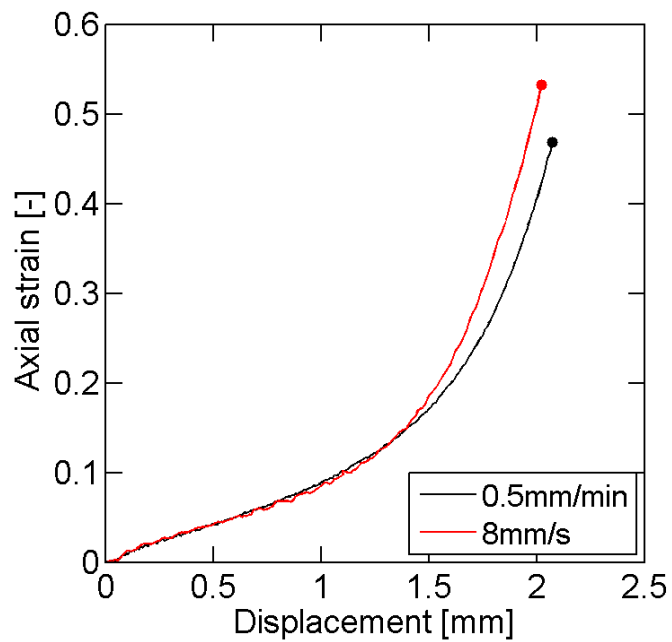
(a)

(b)

Figure 4-3: Experimental results of notched tensile specimens with a 20mm radius. (a) Force displacement curves and (b) Evolution of engineering axial surface strain at the center of the gage section. Results for low strain rates are shown in black, intermediate strain rates in red and high strain rates in blue. Solid dots correspond to the onset of fracture.

(a)

(b)

Figure 4-4: Experimental results of notched tensile specimens with a 6.65mm radius. (a) Force displacement curves and (b) Evolution of engineering axial surface strain at the center of the gage section. Results for low strain rates are shown in black, intermediate strain rates in red and high strain rates in blue. Solid dots correspond to the onset of fracture.

load carrying capacity is about 13% for all strain rates. In case of the 6.65mm geometry
(Fig. 4-4a), however, the force drop before fracture increases with strain rate, from 6%
at low strain rate to 15% at high strain rate. Note that the onset of necking has a non-
monotonic dependence to strain rate. For both geometries, necking occurs at a lower
displacement at intermediate strain rate than at low strain rate, and at a higher
displacement at high strain rate than at intermediate strain rate.

The evolutions of axial surface strain, depicted in Figs. 4-3b and 4-4b for the
20mm and 6.65mm geometries, show a pronounced increase of axial surface strain
rate, which corresponds to localization of the plastic flow. Note that the slope of the
curves plotted in Figs. 4-3b and 4-4b does not correspond, but is proportional to
engineering strain rate as low and intermediate strain rate experiments are run at almost
constant imposed velocity. The change of slope occurring earlier in the intermediate
experiments (in red in Figs. 4-3b and 4-4b) confirms that necking happens at a lower
displacement at intermediate strain rate than at low strain rate. A noticeable difference
between the two geometries concerns the surface strain reached at the onset of fracture
at the center of the gage section. With a notch radius of 20mm (Fig. 4-3b), the surface
axial strain at fracture is lower by 7% at intermediate strain rate ($\varepsilon = 0.67$) than at low
strain rate ($\varepsilon = 0.72$), whereas it is higher by 13% at intermediate strain rate ($\varepsilon = 0.53$)
than at low strain rate ($\varepsilon = 0.47$) with a 6.65mm notch radius (Fig. 4-4b).

4.4 Rate- and temperature-dependent plasticity modeling

4.4.1 Constitutive equations

A phenomenological approach is taken to model the material behavior. The
material state is described through the Cauchy stress tensor $\boldsymbol{\sigma}$ and the absolute
temperature θ, in conjunction with a set of internal variables: the plastic strain tensor
$\boldsymbol{\varepsilon}^{\boldsymbol{p}}$, the equivalent plastic strain rate $\dot{\bar{\varepsilon}}^{p}$ and a hardening variable s representing the
material resistance to plastic deformation.

Incremental plasticity, based on an additive decomposition of the logarithmic strain tensor $\boldsymbol{\varepsilon}$ is employed

$$\boldsymbol{\varepsilon} = \boldsymbol{\varepsilon}^e + \boldsymbol{\varepsilon}^p \tag{4-2}$$

The constitutive equation for stress classically reads

$$\boldsymbol{\sigma} = \boldsymbol{C}_{el} : \boldsymbol{\varepsilon}^e \tag{4-3}$$

where $\boldsymbol{C}_{el}$ is the fourth-order isotropic elasticity tensor, characterized by the Young's modulus E and the Poisson ratio ν. The effect of thermal expansion is neglected in this work.

The magnitude of the Cauchy stress is characterized by the equivalent stress

$$\bar{\sigma} = \mathcal{F}(\boldsymbol{\sigma}) \tag{4-4}$$

while the flow rule describing the evolution of the plastic strain tensor is defined as

$$\dot{\boldsymbol{\varepsilon}}^p = \dot{\lambda} \frac{\partial \mathcal{G}}{\partial \boldsymbol{\sigma}} \tag{4-5}$$

where $\dot{\lambda}$ is a plastic multiplier, and $\mathcal{G}(\boldsymbol{\sigma})$ represents the plastic potential. Note that when $\mathcal{F} = \mathcal{G}$, Eq. 4-5 corresponds to an associated flow rule, while non-associated flow is modeled otherwise.

The equivalent plastic strain rate $\dot{\bar{\varepsilon}}^p$ is defined as the work-conjugate to the equivalent stress

$$\mathcal{D} = \bar{\sigma} \dot{\bar{\varepsilon}}^p = \boldsymbol{\sigma} : \dot{\boldsymbol{\varepsilon}}^p \tag{4-6}$$

where $\mathcal{D}$ is the rate of plastic work. Upon evaluation of this relationship for the plastic flow defined in Eq. 4-5, we obtain the following relationship between the equivalent plastic strain rate and the plastic multiplier

$$\dot{\bar{\varepsilon}}^p = \dot{\lambda} \frac{\mathcal{G}}{\mathcal{F}} \tag{4-7}$$

The choice of an associated flow rule yields $\dot{\bar{\varepsilon}}^p = \dot{\lambda}$.

The rate and temperature sensitivity of the material behavior is introduced through the relationship

$$\dot{\bar{\varepsilon}}^p = f(\bar{\sigma}, s, \theta) \tag{4-8}$$

Finally the material hardening during straining is described by the evolution equation

$$\dot{s} = g(\bar{\sigma}, s, \theta) \tag{4-9}$$

Since this work focuses on monotonic loadings only, kinematic hardening is not considered.

In high strain rate deformation processes, the material is submitted to a temperature increase due to quasi-adiabatic heating. For the adiabatic case, the temperature rises according to

$$\rho c \dot{\theta} = \zeta \bar{\sigma} \dot{\bar{\varepsilon}}^p \tag{4-10}$$

Where ρ is the density, c the specific heat and ζ the ratio of plastic work converted to heat. Typically a value of $\zeta = 0.9$ is used (Rusinek and Klepaczko, 2009, [156]).

4.4.2   Model specialization

The constitutive model defined in Section 4.4.1 is fully characterized by the four functions $\mathcal{F}(\boldsymbol{\sigma})$, $\mathcal{G}(\boldsymbol{\sigma})$, $f(\bar{\sigma}, s, \theta)$ and $g(\bar{\sigma}, s, \theta)$. Specific forms permitting to model accurately the plastic behavior of the TRIP material are given thereafter.

4.4.2.1   Equivalent stress and flow potential

For the present sheet material, nearly the same stress-strain curve is measured in uniaxial tension for different specimen orientations even though the Lankford coefficients are direction dependent. As detailed in Mohr et al. (2010, [122]), we therefore make use of planar isotropic quadratic yield function, along with a non-associated flow rule based on a quadratic anisotropic flow potential.

$$\mathcal{F} = \sqrt{(\boldsymbol{F\sigma}) \cdot \boldsymbol{\sigma}} \tag{4-11}$$

and

$$\mathcal{G} = \sqrt{(\boldsymbol{G\sigma}) \cdot \boldsymbol{\sigma}} \tag{4-12}$$

F and **G** are symmetric positive-semidefinite matrices, with $\mathcal{F} = 0$ and $\mathcal{G} = 0$ if and only if $\boldsymbol{\sigma}$ is a hydrostatic stress state. $\boldsymbol{\sigma}$ denotes the Cauchy stress vector in material coordinates,

$$\boldsymbol{\sigma} = [\sigma_0 \quad \sigma_{90} \quad \sigma_n \quad \tau \quad \tau_{0n} \quad \tau_{90n}]^T \tag{4-13}$$

The components σ_0, σ_{90} and σ_n represent the true normal stress in the rolling, transverse and out-of-plane directions; τ denotes the corresponding in-plane shear stress, while τ_{0n} and τ_{90n} represent the corresponding out-of-plane shear stresses. Note that in the specific case of quadratic stress and flow potentials defined by Eq. 4-11 and 4-12, Stoughton (2002, [164]) demonstrated that the non-associated flow rule is consistent with laws of thermodynamics. As shown in Mohr et al. (2010, [122]), the matrices **F** and **G** have only 3 independent coefficients: F_{12}, F_{22} and F_{33}, G_{12}, G_{22} and G_{33}.

4.4.2.2   Strain hardening

A review of existing strain hardening functions g and rate sensitivity functions f, governing $\dot{s}$ and $\dot{\bar{\varepsilon}}^p$ respectively, can be found in Sung et al. (2010, [169]). Here, the hardening modulus $h = \partial s / \partial \varepsilon$ is considered as stress- and temperature- independent. Equation 4-9 can therefore be reduced to

$$\dot{s} = h(s)\dot{\bar{\varepsilon}}^p \tag{4-14}$$

Among the numerous hardening laws present in the literature, a saturation hardening law is selected as it can account for large hardening capabilities of TRIP steels at low strains as well as a vanishing hardening at very high strains,

$$h(s) = H_0 \left(1 - \frac{s}{s_\infty}\right)^r \qquad (4\text{-}15)$$

4.4.2.3   Strain rate and temperature sensitivity

A constitutive relation derived from the Mechanical Threshold Stress theory (MTS; Follansbee and Kocks, 1988, [58]) is chosen to describe the dependence of the equivalent plastic strain rate $\dot{\bar{\varepsilon}}^p$ to the applied stress $\bar{\sigma}$, the deformation resistance s and temperature θ. This physics-inspired plasticity model considers dislocation motion as the only source of plastic deformation and describes it as a thermally activable process.

The deformation resistance to dislocation motion s is conceptually decomposed into two parts,

$$s = s_{th} + s_a \qquad (4\text{-}16)$$

where s_a represents the part of resistance due to athermal obstacles (typically long range obstacles such as grain boundaries or large precipitates) and s_{th} represents the part of the resistance due to thermally activable obstacles which can be overcome by thermal fluctuations (typically short range obstacles such as the Peierls resistance, forest dislocations or solute atoms). Therefore, a lower stress is required to overcome the short range resistance s_{th} at higher temperatures. Introducing an effective "thermal" stress

$$\bar{\sigma}_{th} = \bar{\sigma} - s_a \qquad (4\text{-}17)$$

then the rate of deformation is described by an Arrhenius expression of the form (Conrad, 1964, [38])

$$\dot{\bar{\varepsilon}}^p = f(\bar{\sigma}, s, \theta) = \begin{cases} 0 & \text{if } \bar{\sigma}_{th} \leq 0 \\ \dot{\varepsilon}_0 \exp\left\{-\dfrac{\Delta G(\bar{\sigma}_{th}, s_{th})}{k_B \theta}\right\} & \text{if } 0 < \bar{\sigma}_{th} \leq s_{th} \end{cases} \qquad (4\text{-}18)$$

where $\dot{\varepsilon}_0$ is a material constant, k_B the Boltzmann's constant and ΔG is the Gibbs' free energy required to overcome the obstacles to dislocation motion with an applied stress, which is phenomenologically modeled as (Kocks et al., 1975, [95])
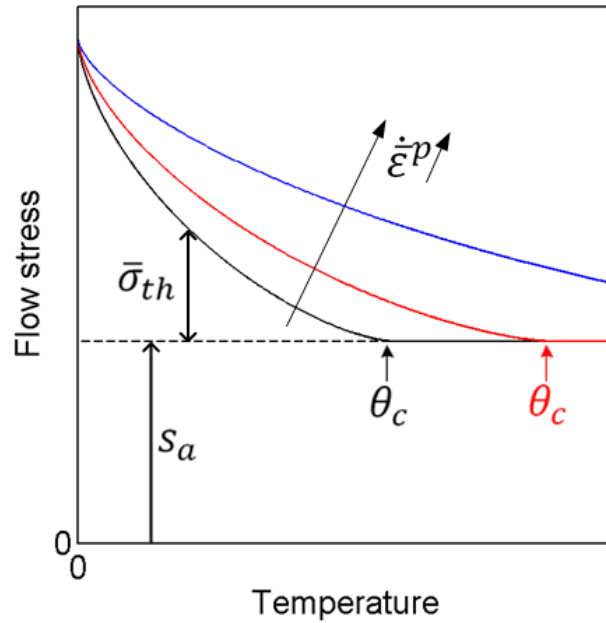
Figure 4-5: Dependence of flow stress to temperature for low strain rate (in black), intermediate strain rate (in red) and high strain rate (in blue), at fixed deformation resistance s. θ_c is the temperature, depending on strain rate, above which there is enough thermal energy to overcome short range barriers by thermal activation only.

$$\Delta G(\bar{\sigma}_{th}, s_{th}) = \Delta F \left[1 - \left(\frac{\bar{\sigma}_{th}}{s_{th}} \right)^p \right]^q \tag{4-19}$$

ΔF is the activation free energy required to overcome the obstacles to dislocation motion without the aid of an applied stress.

Strain hardening of the material can be described either by an increase of s_a (e.g. Kothari and Anand, 1998, [98]), of s_{th} (e.g. Follansbee and Kocks, 1988, [58]) or both (e.g. Balasubramanian and Anand, 2002, [8]) during plastic loading. Here we assume that both s_a and s_{th} increase at the same rate: the ratio $\chi = s_{th}/s_a$ is kept constant throughout loading. Therefore, Eq. 4-18 can be rewritten as

$$\bar{\sigma} = s_a + Z(\dot{\bar{\varepsilon}}^p, \theta) s_{th} = \frac{1 + \chi Z(\dot{\bar{\varepsilon}}^p, \theta)}{1 + \chi} s \tag{4-20}$$

where

$$Z = \left\{ 1 - \left[\frac{\theta}{\theta_c(\dot{\bar{\varepsilon}}^p)} \right]^{\frac{1}{q}} \right\}^{\frac{1}{p}} \leq 1 \quad \text{with} \quad \theta_c = \frac{\Delta F}{k_B \ln\left(\dot{\varepsilon}_0 \big/ \dot{\bar{\varepsilon}}^p \right)} \tag{4-21}$$

Figure 4-5 depicts the dependence of the flow stress to temperature for different strain rates. As detailed in Balasubramanian and Anand (2002, [8]), θ_c is the critical temperature above which there is enough thermal energy for the barriers to be overcome by thermal fluctuation only, without applying stress. Therefore, at a given equivalent plastic strain rate $\dot{\bar{\varepsilon}}^p$, the temperature $\theta_c(\dot{\bar{\varepsilon}}^p)$ is the limit of applicability of this plasticity model.

4.4.3   Calibration procedure

The rate- and temperature- dependent constitutive model defined in Sections 4.4.1 and 4.4.2 features 17 independent material parameters overall: 2 elastic coefficients, 3 coefficients defining the equivalent stress function $\mathcal{F}$ (Eq. 4-11), 3 coefficients defining the plastic flow potential $\mathcal{G}$ (Eq. 4-12), 4 coefficients defining the strain hardening function g (Eq. 4-15) and 5 coefficients defining the rate sensitivity function f (Eq. 4-18). The calibration procedure is given thereafter. The set of parameters calibrated for the present TRIP material are given in Table 4-1.

The equivalent stress function $\mathcal{F}$ and plastic flow potential $\mathcal{G}$ are calibrated based on uniaxial tension experiments carried out at low strain rate. Corresponding matrices **F** and **G** are calibrated following the procedure described in Mohr et al. (2010, [122]). Since the spacial resolution of high speed imaging system is not sufficient to measure the Lankford coefficients in high strain rate tension experiments, it is assumed that the anisotropy of the plastic flow observed at low strain rate is independent from the strain rate. The flow potential $\mathcal{G}$ is therefore assumed rate-independent. Note that because of a lack of experimental data characterizing the out-of-plane behavior of the sheet material, coefficients of **F** and **G** corresponding to out-of-plane shear are set equal to 3 (isotropic value).

An optimization based inverse method is carried out to calibrate the coefficients of the strain hardening and rate sensitivity functions. The objective of the optimization

Table 4-1: Material parameters for the rate-dependent model

Elastic constants		Strain hardening parameters			
E [MPa]	v [-]	s_0 [MPa]	s_∞ [MPa]	H_0 [MPa]	r [-]
185,000	0.3	503	1,383	41,505	2.513

Strain rate sensitivity parameters				
$\dot{\varepsilon}_0$ [s^{-1}]	ΔF [J]	p [-]	q [-]	χ [-]
67,457	8.794E-20	1.911	1.861	0.1949

| Equivalent stress and flow potential parameters						
F_{11} [-]	F_{22} [-]	F_{33} [-]	F_{44} [-]	F_{12} [-]	F_{13} [-]	F_{23} [-]
1	1	1.076	2.925	-0.462	-0.538	-0.538
G_{11} [-]	G_{22} [-]	G_{33} [-]	G_{44} [-]	G_{12} [-]	G_{13} [-]	G_{23} [-]
1	0.873	1.071	3.13	-0.401	-0.599	-0.472

process is to find the set of parameters that leads to the best prediction of the force-displacements curves of the notched tensile specimen with a 6.65mm radius measured in low, intermediate and high strain rate experiments. For a given set of parameters $\boldsymbol{\alpha}$, numerical simulations of the 6.65mm notched tensile specimen are carried out for the three different strain rates, using the Finite Element model described in Section 4.5.1. Then the three predicted force-displacement curves are compared to experimental measurements up to the fracture displacement u_f to evaluate the cost function E for the set of parameters $\boldsymbol{\alpha}$

$$E^2(\boldsymbol{\alpha}) = \sum_N \left\{ \frac{1}{u_f} \int_0^{u_f} \eta(u)[F_{FEA}(u) - F_{EXP}(u)]^2 \, du \right\} \tag{4-22}$$
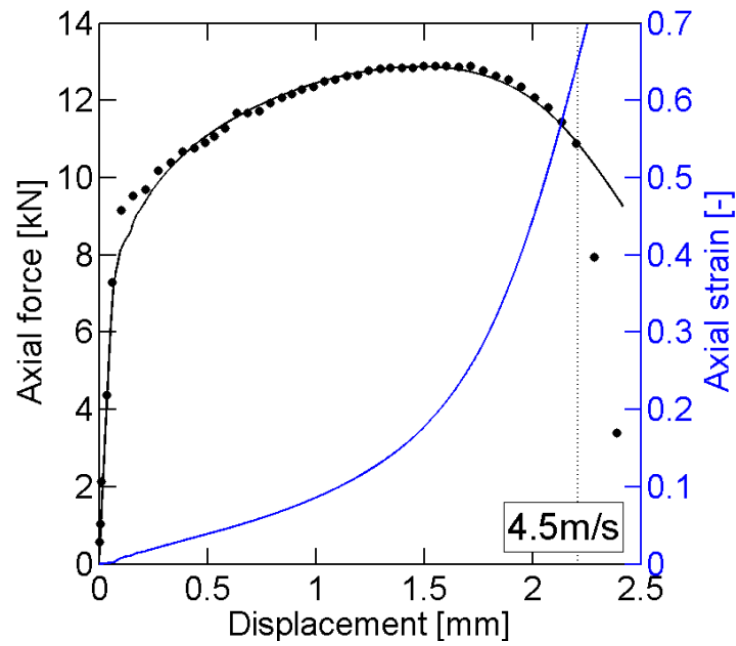
where $N = 3$ is the number of calibration tests and η is a weighting factor used to focus the fitting process on the part of the force-displacement curves located between maximum force and the onset of facture. Before maximum force is reached $\eta = 1$,
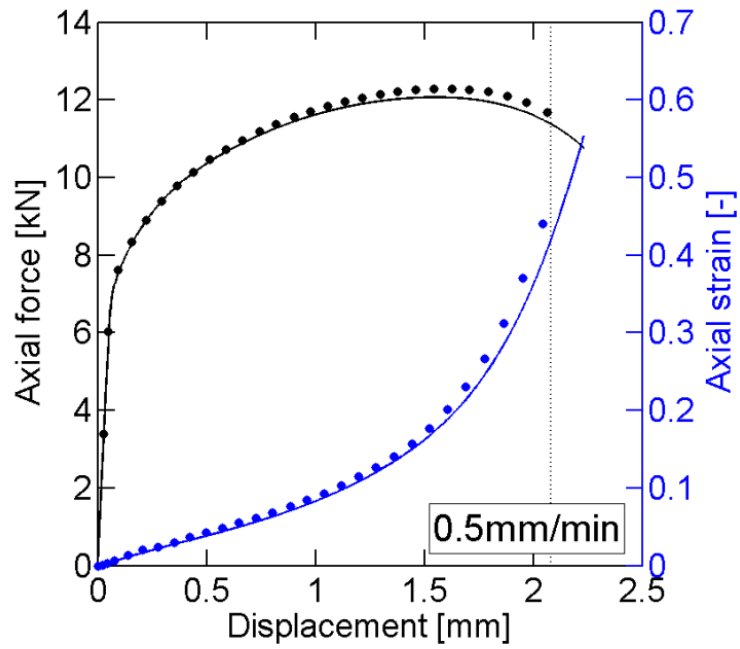
(a)
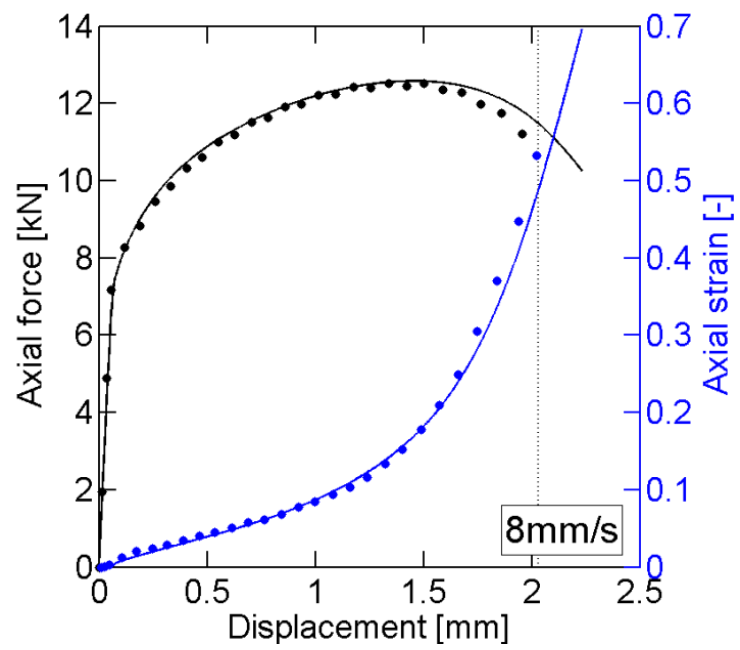
(b)

(c)

Figure 4-6: Experimental (points) and simulation (solid curves) results for the notched tensile specimen with a $R = 6.65mm$ radius, at (a) low, (b) intermediate and (c) high strain rate. Force displacement curves are in black and engineering axial strain versus displacement curves in blue. The dashed lines depict the instant of fracture.

while $\eta = 5$ beyond maximum force. A downhill simplex minimization algorithm (Nelder and Mead, 1965, [133]) is used to find the set of parameters $\boldsymbol{\alpha_{min}}$ that minimizes E, as it requires the evaluation of the error function only, but not its derivatives

$$\boldsymbol{\alpha_{min}} = \operatorname*{argmin}_{\boldsymbol{\alpha}} E(\boldsymbol{\alpha}) \tag{4-23}$$

Overall 640 iterations were required to converge to a minimum. Corresponding force displacement curves are shown in Fig. 4-6. Numerical predictions (solid black lines in Fig. 4-6) are in very close agreement with experimental results (black dots in Fig. 4-6) for all three strain rates, including after the maximum of force is reached. Note that the resulting set of optimal parameters, given in Table 4-1, corresponds only to a local minimum of the error function E. This optimal set might not be the unique set of parameters minimizing E, and it is not necessarily the best possible set (absolute minimum of E).

4.5   Numerical analysis and plasticity model validation

4.5.1   Finite element model

Dynamic explicit simulations of each tensile experiment are carried out using the commercial Finite Element Analysis package Abaqus (2011, [1]). The constitutive model described in Section 4.4 is implemented as a user material through the VUMAT interface (see Appendix A for details on the implementation). Specimens are meshed with reduced integration brick elements with a temperature degree of freedom (type C3D8RT of the Abaqus library). Exploiting the symmetry of the notched specimen geometries, material properties and loading conditions, only one eighth of the notched specimens are modeled: the mesh represents the upper right quarter of the tensile specimens, with half the thickness. The distance between the center of the gage section and the upper mesh boundary corresponds exactly to half the length of the virtual extensometer used to measure displacements during the experiments. Note that experimental observations demonstrate that plastic localization also respects the specimen symmetries. Reduced meshes can therefore be used to model the post-necking behavior of notched tensile specimens. In uniaxial tension experiments, however, so-called diffuse necking leads to a slanted band of plastic localization that does not respect the initial symmetries. The meshes used for uniaxial tension model the full specimen geometries, including the specimen shoulders.

In all tensile experiments carried out, the plastic flow localizes before the onset of fracture, leading to steep gradients of stresses and strains both in-plane and through the sheet thickness. To capture accurately the post-necking behavior, a fine mesh featuring 8 elements through the half-thickness and an element in-plane dimension of 0.1mm at the center of the gage section is used (see Chapter 5 for details).

Simulations of each loading condition are performed. For that purpose half the experimental velocity measured by DIC is uniformly imposed to the upper boundary of the mesh. A zero normal displacement condition is imposed to boundaries corresponding to symmetry planes. Simulations are run slightly beyond the displacement at which fracture occurs in the experiment. To speed up calculations, uniform mass scaling is used in the low strain rate simulations. The material density is

artificially adjusted to reach the fracture displacement within 300,000 time increments. High strain rate experiments are simulated with the real material density (7.8g/cm^3), resulting in an initial stable time increment of 1.1×10^{-8}s and about 50,000 increments.

To account for both temperature increase due to plastic work and heat diffusion due to temperature gradients, the "temperature-displacement analysis" capability of the Abaqus/Explicit solver is used to simulate the intermediate and high strain rate experiments. In this type of Finite Element analysis, both the equilibrium and heat transfer equations are solved. Since most plastic deformation and thus most heat generation are localized at the center of the gage section, no heat flow is modeled on the upper boundary of the mesh. In addition, a no heat flow condition is also imposed to the boundaries corresponding to symmetry planes. Furthermore, no heat transfer is considered at the specimen surface. A material specific heat of 490 J/K/kg and a conductivity of 45 J/s/m/K are chosen. Low strain rate experiments are modeled as isothermal.
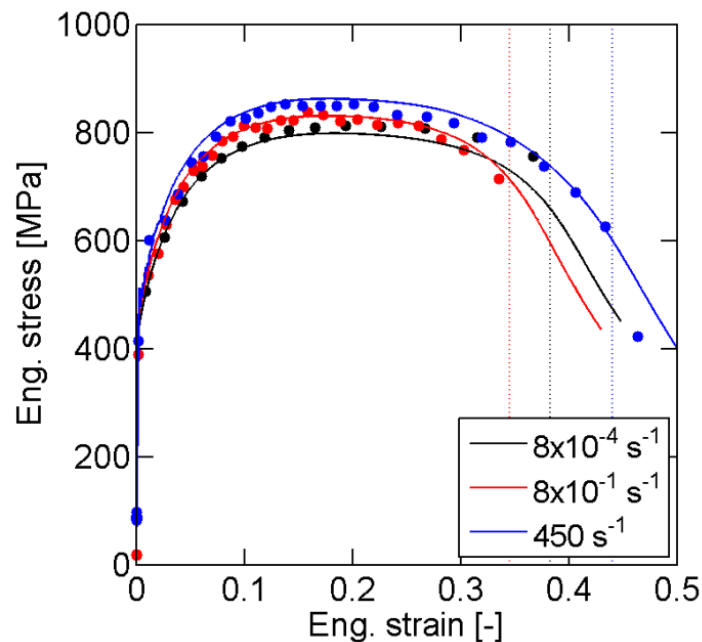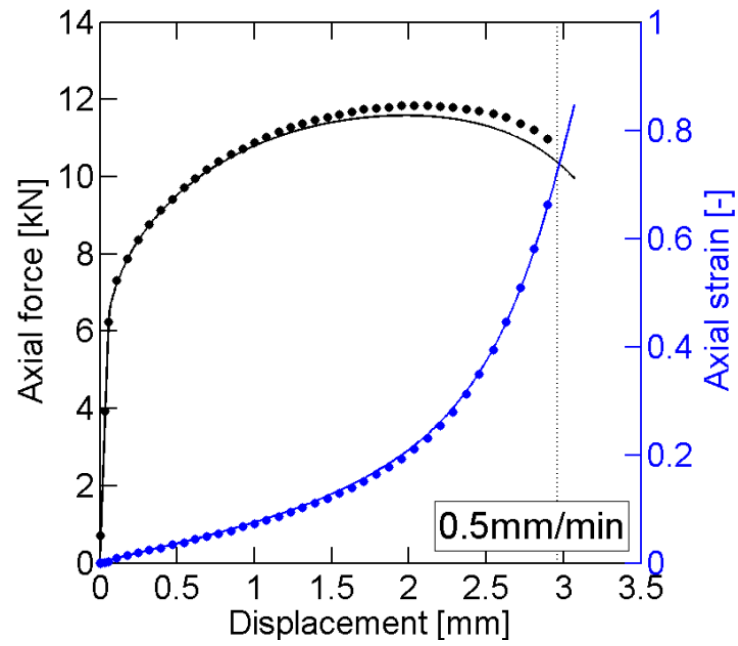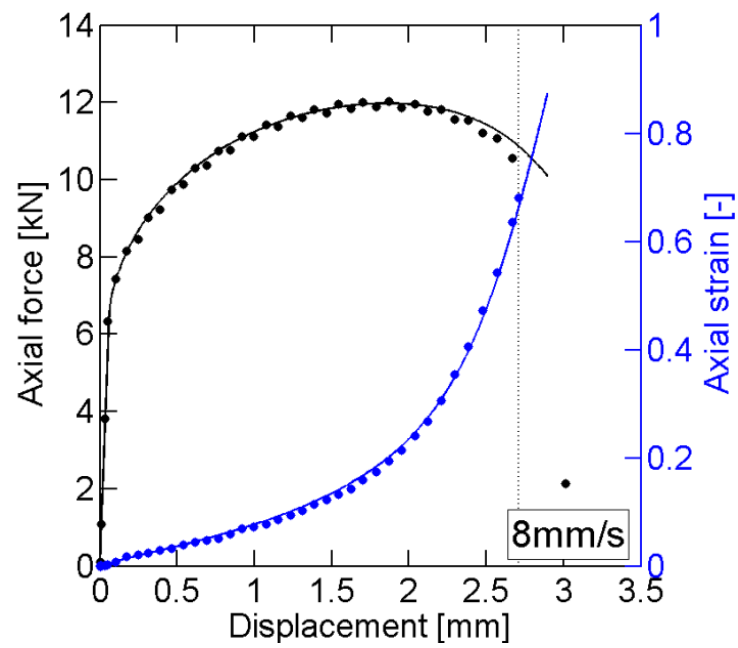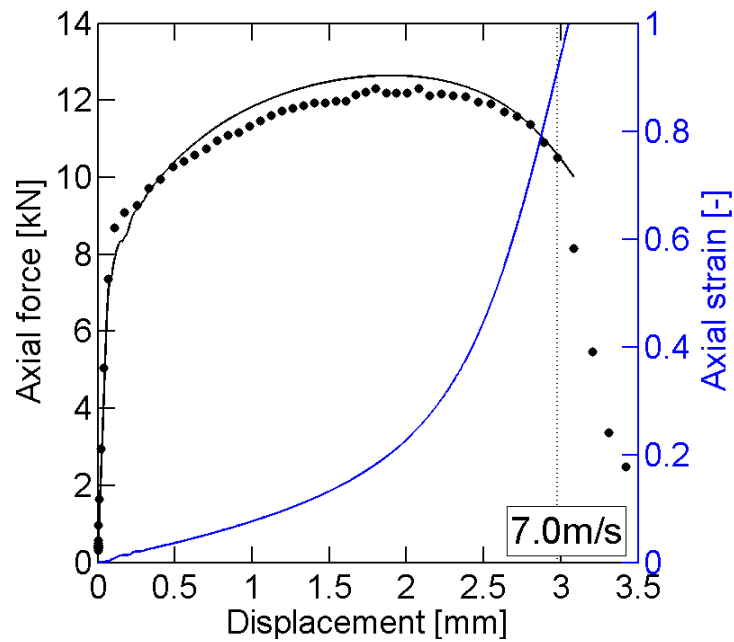

Figure 4-7: Experimental (points) and simulation (solid curves) results for uniaxial tension at low (black curve), intermediate (red curve) and high strain rate (blue curve). The dashed lines depict the instant of fracture.

(a)

(b)

(c)

Figure 4-8: Experimental (points) and simulation (solid curves) results for the notched tensile specimen with a $R = 20mm$ radius, at (a) low, (b) intermediate and (c) high strain rate. Force displacement curves are in black and central logarithmic axial strain versus displacement curves in blue. The dashed lines depict the instant of fracture.

4.5.2 Comparison of numerical and experimental results

Figures 4-6 to 4-8 present a comparison between results from numerical simulations (solid lines) of all tensile experiments and experimental measurements (solid dots). The instant of the onset of fracture is depicted for all experiments through a vertical dashed line. Recall that only the force-displacement curves of the 6.65mm notched tensile experiments (in black in Fig. 4-6) are used to calibrate the proposed plasticity model. All other results may be seen as model validation.

Uniaxial engineering stress strain curves are shown in Fig. 4-7. The numerical engineering strain is computed according to Eq. 4-1 from the displacements of nodes positioned at the same location as DIC reference points, while the numerical engineering stress is obtained from the force applied at the specimen boundaries normalized by the gage section initial cross section area. Experimental results at both intermediate (in red in Fig. 4-7) and high strain rate (in blue in Fig. 4-7) are extremely

well predicted, as numerical results (solid lines) and experimental measurements (solid dots) lie almost exactly on top of each other up to fracture. Note that the loss of load carrying capacity preceding fracture is correctly predicted in both cases. Concerning the low strain rate experiment (in black in Fig. 4-7), the stress strain curve is well predicted in the range of uniform elongation (before maximum engineering stress is reached). However, the force level is underestimated after the onset of necking, resulting in a predicted force 7% lower than the experimental one at the onset of fracture.

In Fig. 4-8, we show the simulated force-displacement curves (solid black lines) of the 20mm notch geometry for low (Fig. 4-8a), intermediate (Fig. 4-8b) and high (Fig. 4-8c) strain rates. The agreement with experimental results is very good all the way to the onset of fracture. The relative difference between experimental and predicted forces does not exceed 3%.

The comparison of the evolution of the surface axial strain at the center of the gage section of notched specimens with respect to the displacement (depicted in blue in Figs. 4-6 and 4-8) also shows a good agreement. Irrespective of the notch radius and the strain rate, the simulations are able to describe the characteristic increases in strain rates that have been observed in the experiments. Relative differences between simulation and DIC strains in case of the 6.65mm notch geometry are about 5% at low strain rate (Fig. 4-6a) and 6% at intermediate strain rate (Fig. 4-6b) at the onset of fracture. For the 20mm notch geometry (Fig. 4-8), the computed strain almost exactly corresponds to the DIC strain, with less than 1% relative error for both strain rates.

4.6   Loading histories to fracture

Stress and strain fields are heterogeneous both in-plane and through the thickness in all experiments performed, because of specimen geometries and plastic flow localization through necking. It is therefore not possible to obtain an accurate estimate of the evolution of stress, strain and strain rate up to fracture from either global (force-displacement curve) or local (surface strains from DIC) experimental measurements (Dunand and Mohr, 2010, [48]). Instead the evolutions of stress state, strain and strain rate are obtained from the Finite Element simulations presented in Section 4.5. From

each simulation, the loading histories are extracted from the integration point where the equivalent plastic strain is highest at the onset of fracture, which is thereby assumed to be the location where fracture initiates. Recall that the onset of fracture is considered to be reached in the simulation when the imposed displacement corresponds to the experimentally measured displacement at which a first crack appears at the specimen surface.

Figures 4-9 to 4-11 summarize the loading histories to fracture in all experiments. The evolutions of strain rate and stress state are shown in Figs. 4-9 and 4-10, respectively. Figure 4-11 depicts the evolution of the equivalent plastic strain versus stress state for all geometries and loading conditions.

The plastic localization associated with necking has a profound influence on the local material state. Despite constant velocities applied to the specimen boundaries, the local strain rate dramatically increases after the onset of necking. In the 20mm notch specimens, the equivalent plastic strain rate is 20 times larger at the onset of fracture than before the onset of necking. In the low strain rate experiment, the strain rate increases from $5\text{x}10^{-4}\text{s}^{-1}$ to 10^{-2}s^{-1} (black line in Fig. 4-9b). The increase ranges from 0.53s^{-1} to 10.5s^{-1} in the intermediate strain rate experiment (in red in Fig. 4-9b) and from 500s^{-1} to $10.2\text{x}10^{3}\text{s}^{-1}$ in the high strain rate experiment (in blue in Fig. 4-9b). Similar increases of strain rates are observed in the 6.65 notch experiment (Fig. 4-9c). In uniaxial tension experiments (Fig. 4-9a), the increase of strain rate due to necking is even more pronounced. In the low strain rate loading (in black in Fig. 4-9a), the equivalent plastic strain rate is 40 times larger at the onset of fracture ($\dot{\bar{\varepsilon}}^p=3.2\text{x}10^{-2}\text{s}^{-1}$) than before necking ($\dot{\bar{\varepsilon}}^p=8\text{x}10^{-4}\text{s}^{-1}$).

Figure 4-10 depicts the stress state trajectory in the (η, ξ) space for the three low strain rate experiments, while the loading trajectories in the $(\eta, \bar{\varepsilon}^p)$ space and the $(\xi, \bar{\varepsilon}^p)$ space are shown for all experiments in Fig. 4-11a and 4-11b respectively. Solid points in Figs. 4-10 and 4-11 mark the onset of fracture. Even though experiments are performed on a sheet material, the stress states at fracture (solid dots in Fig. 4-10) significantly differ from the plane stress condition (represented by a dashed line in Fig. 4-10). After the onset of necking, the triaxiality increases (Fig. 4-11a) and the third invariant decreases (Fig. 4-11b) continuously in all experiments. In the specific case of
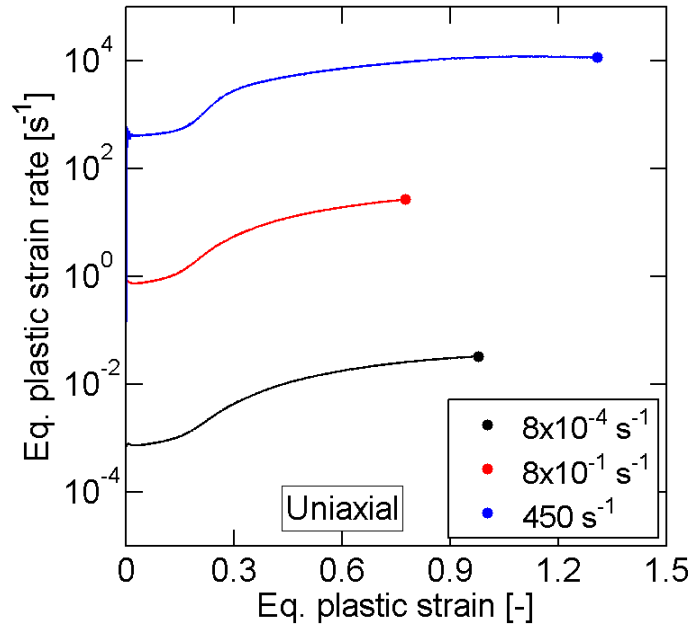
(a)
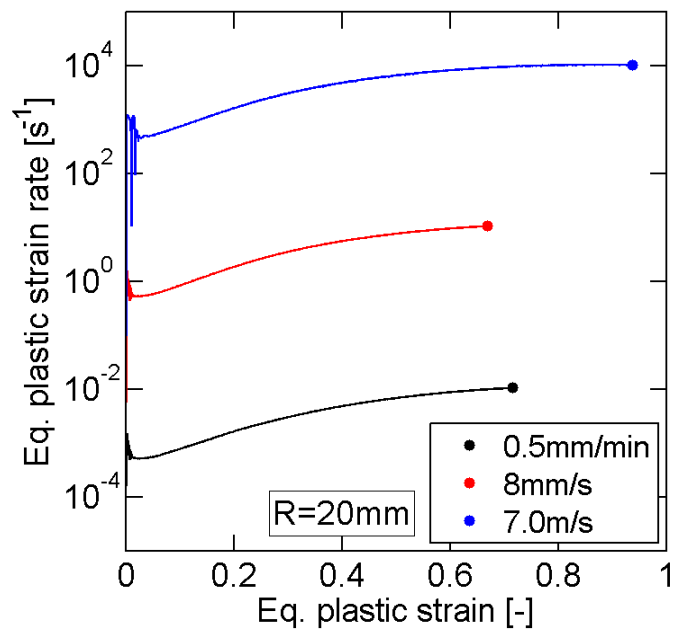
(b)
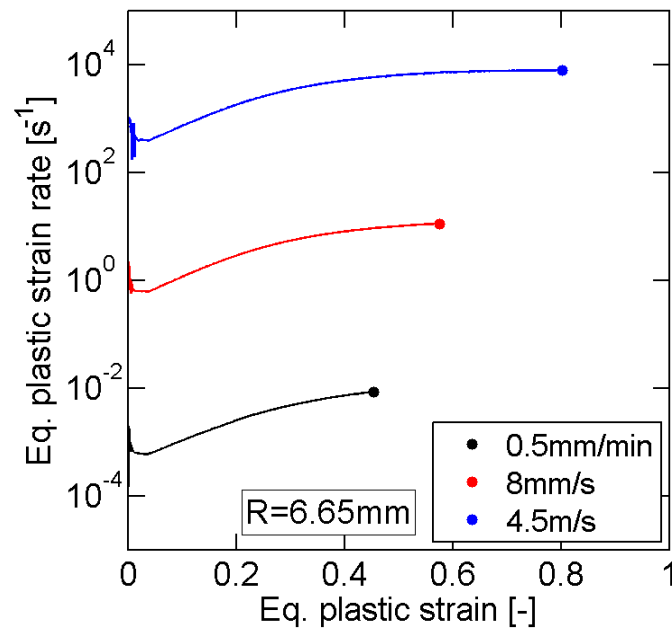
(c)

Figure 4-9: Numerical prediction of the evolution of equivalent plastic strain rate versus equivalent plastic strain at the location where fracture is assumed to initiate in (a) uniaxial tension, (b) 20mm notch tension and (c) 6.65mm notched tension experiments. Solid dots indicate the onset of fracture.

uniaxial tension at high strain rate, the triaxiality ramps up from $\eta = 0.33$ to $\eta = 0.85$ while the third invariant decreases from $\xi = 1$ down to $\xi = 0.26$.

The equivalent plastic strain reached at the onset of fracture, or fracture strain ε_f, strongly depends on both the stress state and the strain rate. In a given range of strain rate, the fracture strain monotonically decreases when moving from uniaxial tension to TPS tension. At low strain rate (black curves in Fig. 4-11), the fracture strain is 60% higher in the 20mm notch specimen ($\varepsilon_f = 0.72$) and 118% higher in the uniaxial specimen ($\varepsilon_f = 0.98$) than in the 6.65mm notch specimen ($\varepsilon_f = 0.45$). The dependence of the fracture strain to strain rate appears to be stress state dependent. In case of the 6.65mm notch specimen, it increases monotonically with strain rate, from $\varepsilon_f = 0.45$ to $\varepsilon_f = 0.58$ at intermediate strain rate and $\varepsilon_f = 0.80$ at high strain rate. In the case of 20mm notch tension specimens, however, the dependence is non-monotonic. The fracture strain at intermediate strain rate ($\varepsilon_f = 0.67$) is lower than at
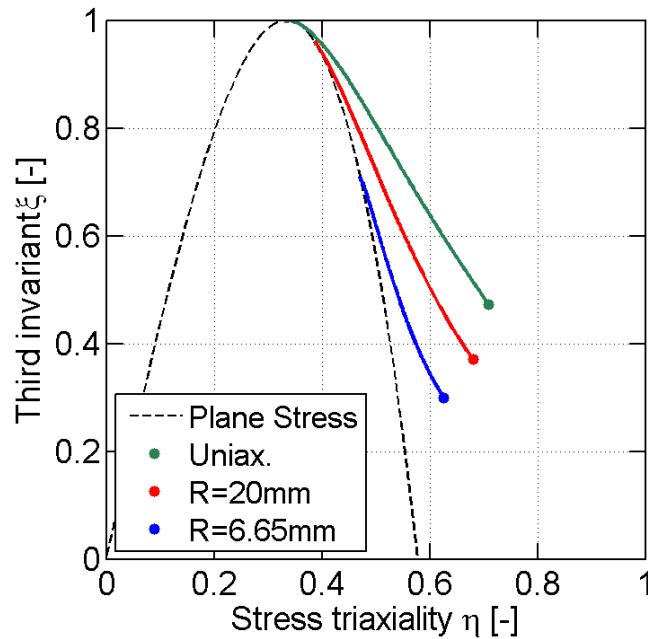
Figure 4-10: Loading path in the (η, ξ) plane for low strain rate experiments. Solid dots indicate the instant of fracture. The black dashed line shows the relation between stress triaxiality and third stress invariant in case of plane stress condition.

low strain rate ($\varepsilon_f = 0.72$) by 7%, but it is highest at high strain rate ($\varepsilon_f = 0.94$). The effect of strain rate is even more pronounced with the uniaxial tension specimen, in which the fracture strain at intermediate strain rate ($\varepsilon_f = 0.77$) is lower than at low strain rate ($\varepsilon_f = 0.98$) by 21%, while it is higher at high strain rate ($\varepsilon_f = 1.31$) by 34%.

Note that for a given geometry, the stress state evolution is more or less independent from the strain rate, as shown in Fig. 4-11. Differences in the fracture strain for different loading conditions on a given specimen are therefore attributed to the dependence of the material ductility to strain rate, and not to a variation in the stress state evolution.
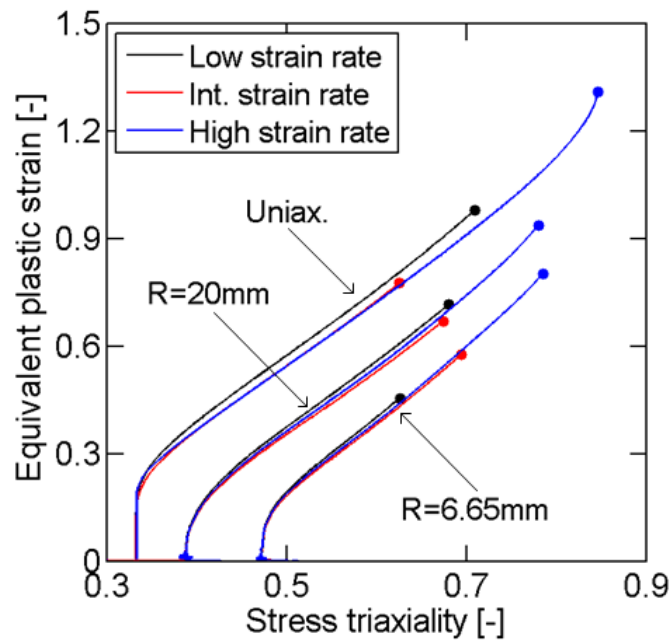
(a)
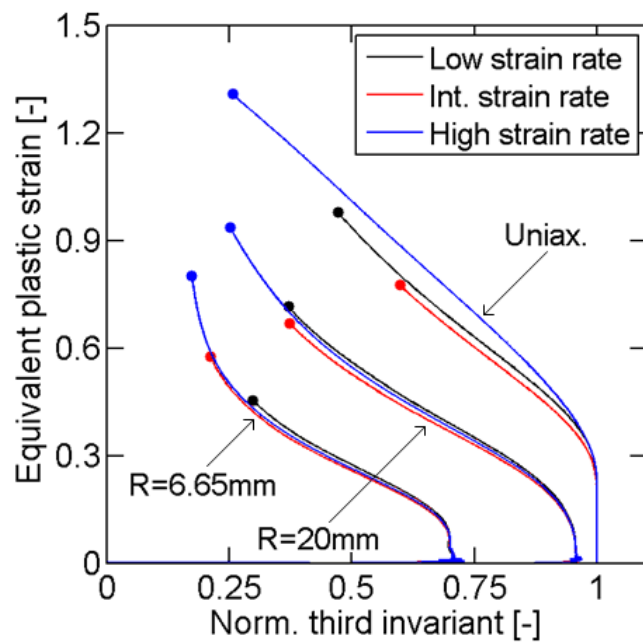
(b)

Figure 4-11: Loading paths to fracture at low (black lines), intermediate (red lines) and high strain rate (blue lines). (a) Evolution of equivalent plastic strain versus stress triaxiality and (b) evolution of equivalent plastic strain versus normalized third stress invariant in all experiments. Solid points depict the onset of fracture.

4.7 Conclusion

The deformation behavior of TRIP780 steel sheets is investigated for different stress states over a wide range of strain rates. Tensile experiments have been carried on notched specimens as well as on uniaxial specimens, using a hydraulic testing machine (for low and intermediate strain rates) and a Split Hopkinson Pressure Bar system (for high strain rate loadings). Positive, but rather weak, strain rate sensitivity is observed. Constitutive equations derived from the MTS theory are proposed to capture the dependence of the material behavior to strain rate as well as the plastic anisotropy observed at low strain rate. The model is calibrated with an inverse optimization method from the force-displacement response of notched tensile specimens deformed at different strain rates, up to fracture. A comparison between experimental results and detailed Finite Element simulations of all the experiments show that the constitutive model can predict accurately the material behavior over all the range of strain rates and stress states considered. In particular, the material behavior at large strains, after the onset of localized necking, is well captured.

A hybrid experimental-numerical approach is followed to evaluate the material loading histories up to the onset of ductile fracture in all experiments. It is shown that the equivalent strain at the onset of fracture is significantly higher at high strain rate than at low and intermediate strain rates. However, results reveal that the dependence of the fracture strain to strain rate is not similar in all types of experiments carried out. In particular the material ductility is lower at intermediate strain rate than at low strain rate for stress states close to uniaxial tension, while the opposite is observed for stress states close to transverse plane strain tension. As a result, the effects of strain rate and stress state should not be considered separately when developing and calibrating rate-dependent fracture models for AHSS sheets.